Measurement 211 (2023) 112645

Contents lists available at ScienceDirect

Measurement

journal homepage: www.elsevier.com/locate/measurement

Experimental application and accuracy assessment of 2D-DIC in meso-direct-shear test of sandy soil

G. Alhakim [a,b,*], C. Núñez-Temes [a], J. Ortiz-Sanz [a], M. Arza-García [a], Lina Jaber [b], M.L. Gil-Docampo [a]

[a] Civil and Geomatics Research Group, Department of Agroforestry Engineering, University of Santiago de Compostela, Spain
[b] Civil and Environmental Engineering Department. Faculty of Engineering, Beirut Arab University, Lebanon

ARTICLE INFO

Keywords:
Direct shear test
Digital Image Correlation
Strain localization
Shear band
New shear box
Noise-floor

ABSTRACT

The examination of the meso-mechanical properties of soils is fundamental to understand its macro-behaviour. This paper aims to evaluate the potential application of Digital Image Correlation (DIC), an optical image processing approach, in direct shear test (DST) for soils. Hence, a new shear box was designed to investigate the close behaviour of granular materials. The noise-floor and shear displacement accuracy were discussed to assess the reliability of DIC, besides the effectiveness of the new box was also examined. The distribution of the displacements, strains, and shear angle were measured under four different normal stresses. From the results, the immediate settlement, and the dilative behaviour of the sand during shearing were observed. Furthermore, the investigation revealed a strain concentration at the interface between the boxes, where a shear band was formed. The use of DIC opens up new ways in soil mechanics, overcoming some limitations of the conventional DST.

1. Introduction

The direct shear test (DST) is one of the most widely applied laboratory experiments in the field of geotechnical engineering. This testing has many advantages, including the simplicity of set-up and sample preparation, the possibility of being conducted under different conditions, relatively quick test, and with low-cost compared to the tri-axial test. The DST is mainly employed to determine the shear strength and shear properties of a soil. Generally, in geotechnical and foundation engineering, the failure patterns that occur are mostly due to the development of shear stress within the soil mass exceeding its shear strength [1]. Therefore, a deep understanding of the strain localization during failure is an important issue to properly quantify and interpret the response of the soil subjected to a shear load, in order to ensure the safety of the ground material and optimize its behaviour.

However, the DST has some limitations, mainly associated with the non-uniformity of stress and strain within the sample, the imposed stress path and failure plane, and the rotation of the loading head during shearing affecting the shear zone [2–4]. Besides, in DST there is always a certain boundary effect, what is generally considered to be another major limitation of this test. As a result, the internal and boundary deformations of the soil might differ, and the relation can be only modelled under theoretical approaches since it is impossible to visually monitor the behaviour of the material central part. In this sense, DIC not only represents a new tool to assess the mesoscopic performance of the specimen under loading, but also could be a direct way to get insights into the boundary effect. In addition, local strains within this zone cannot be estimated accurately in the conventional DST, as it is not possible to assess the deformation pattern within the shear zone and calculate its thickness [5]. Since this test provides limited information, numerical investigations of DST using Discrete Element Method (DEM) have been employed to simulate the behaviour of granular materials [6–13]. In their reports, the authors presented thorough quantitative studies about the kinematics of the distinct grains, defining the macro behaviour of the soil by investigating the micro and meso-mechanical intergranular properties. These simulations provided insights on the evolution of heterogeneity and anisotropy in the localized shear zones within the samples

Nonetheless, the numerical simulations need experimental explorations to validate the proposed models. Thereby, several research used non-destructive imaging methods to analyze the internal structure and performance of geomaterials. For instance, X-ray tomography has been

* Corresponding author at: Civil and Geomatics Research Group, Department of Agroforestry Engineering, University of Santiago de Compostela, Spain.
E-mail addresses: g.hakim@bau.edu.lb, ghida.alhakim@rai.usc.es (G. Alhakim), carlos.nunez.temes@usc.es (C. Núñez-Temes), juan.ortiz@usc.es (J. Ortiz-Sanz), m.arza@usc.es (M. Arza-García), l.jaber@bau.edu.lb (L. Jaber), ml.gil@usc.es (M.L. Gil-Docampo).

https://doi.org/10.1016/j.measurement.2023.112645
Received 12 October 2022; Received in revised form 19 February 2023; Accepted 20 February 2023
Available online 25 February 2023

adopted to acquire microscopic data on the inner fabric of granular materials [14–19], and rock mass [20]. However, wide adoption of this method is still impractical and costly, as it implies the use of complicated research procedures and highly specialized equipment [21].

A more accessible and affordable approach for noncontact full-field measurement is based on optical remote sensing techniques, that becomes more and more tempting for researchers and testing laboratories worldwide. Digital Image Correlation (DIC) is a key technology within this group, that combines image registration and tracking methods to compute the displacements and deformations of a structural element/material. DIC compares and correlates two recorded images (i.e., reference and deformed) and determines the similarity between them, by considering small subsets where the displacements are going to be estimated. Both images should carry enough optical information and contain unique and identifiable features, hence an explicit matching could be obtained between the reference and deformed subsets. Therefore, grey level textured images with high dynamic range and local contrast are generally required [22]. Some materials show naturally a unique pattern over their surfaces (e.g., rocks and granular soils) that contribute to meeting these requirements. Nonetheless, in other cases, DIC might necessitate an artificial randomized speckle pattern to resolve these issues of contrast and uniqueness (e.g., by spraying the component surface of the tested material with contrasting colour paints).

DIC was first exploited at the University of South Carolina, in the early 80s [23,24], and since then, it has been employed in a large range of domains and research areas. Numerous previous studies employed the DIC technique to investigate the performance of concrete [25–28]. For instance, the DIC technique was applied to examine the cracking process and crack kinematics in prestressed [29], and reinforced [30] concrete beams. Moreover, it was used to measure the fracture properties of reinforced concrete [31], concrete containing fly ash [32], and geopolymeric recycled aggregate concrete [33]. The image-based approach was also used to assess the behaviour of road materials [34–36]. In their works, the authors assured the usefulness and effectiveness of this optical method in testing and observing the behaviour and properties of these materials.

Besides, in geotechnical engineering research, DIC practices were extensively employed to measure the subpixel displacements in soils [37–39], and to explore the crack and failure mechanism in rocks [40–44]. Li et al. (2019) [45] designed a new direct tensile apparatus and exploited DIC to study the deformation and strain fields within clayey soil. They stated that the use of this method is suitable, providing important information on different stages of tensile deformation and strain concentration of the investigated material. Wang et al. (2019) [46] performed a series of plane strain compressive tests on medium dense sandy soil by implementing a new apparatus. The findings revealed that the DIC method achieved reliable results in geotechnical tests.

3D-DIC and photogrammetry-based techniques were also recently applied to the triaxial apparatus to obtain accurate maps of spatial deformation and volumetric strains of the tested specimens [47–53]. The authors authenticated the progress in the image-based methods for soil deformation measurement, which offers significant potential for advanced geomaterials behaviour characterization. However, the DIC application to DST has only a few precedents. Shen et al. [54] carried out DST on calcareous sand with a particles size of 0.5–1 mm, by using a half mold to record and process DIC conventional images. Calcareous sand is a type of marine sediment with high calcium carbonate content, and it is characterized by high porosity, high grain angularity, and brittle behaviour, which make its performance notably different from other soil types. In their study, the authors found that a shear band of a thickness ranging between 0.79 and 1.59 mm was formed during shearing at the interface between the upper and lower shear boxes, where the shear strain was mostly localized. Yet, in this laboratory investigation, they experimented under only one normal stress of 400 kPa. Likewise, Kong et al. [55] employed this optical technique to monitor the DST by cutting one side of the shear box and creating a speckled pattern by applying an artificial paint to the sand particles. Nevertheless, the use of this speckling method could affect the overall behavioral characteristics of the tested soil, particularly the interfacial properties between the painted grains. The results indicated that the maximum shear strain occurred at the junction of the upper and lower shear boxes with a clear formation of a shear band.

The review of literature in broad domains has already proven that the DIC technology is an indispensable and irreplaceable tool for microscale deformation measurements, and it continues to gain burgeoning popularity [56]. Despite this, only a few studies investigated its application on DST as it was documented. Additionally, in the above-mentioned studies applying DIC to DST [54,55], the results are still preliminary as the authors did not carry out an extensive validation of the accuracy of the DIC measures. Hence, it is of great importance to perform an in-depth experimental work to evaluate the meso-properties of sandy soil subjected to direct shear loading, along with a detailed accuracy quantification of the DIC technology. Furthermore, an assessment of employing a newly designed shear box will be investigated including a particular selection of the speckled surface.

The main aim of the present paper is to explore the potential application of DIC in monitoring the DST on sandy soil. For that reason, a new shearing apparatus consisting of a modified carriage and an open shear box by using plexiglass plates was designed. Two validation assessments were discussed to quantify the accuracy of DIC, namely, the noise-floor analysis and the comparison of the measurements with contact methods (i.e., transducers). Moreover, to estimate the effectiveness of the modified apparatus, the lateral deformation of the used plexiglass plate in the new shear box was studied and the rotation of the upper shear box was also examined and compared to the behaviour of the conventional metal device. The full-field measurement of DIC provided suitable means to quantitatively analyze the deformation and strain distribution before and after shearing the specimen. Besides, the obtained localized strains were investigated to examine the progressive shear failure process along with the development of the shear band.

2. Materials and Methods

2.1. Soil

The soil used in the present investigation is siliceous sand. Silica sand has in general more regular particle shape than the calcareous sand, what could represent a drawback for DIC tracking algorithms. Instead, potential fragmentation of the calcareous particles might also introduce correlation issues. According to the Unified Soil Classification System, the soil is classified as poorly graded sand (SP). Fig. 1 shows the particle size distribution and Table 1 presents the main properties of the tested soil, which include the shear strength parameters (c and Φ) according to Mohr-Coulomb failure criterion.

2.2. Sample Preparation

To prepare the sandy samples, the soil was first oven-dried at a temperature of 105 °C for 24 h. Then water was supplemented gradually in the quantity of 10% by dry weight of the soil according to its compaction characteristics and mixed thoroughly with the specimen. The samples were then prepared by using the moist tamping method in correspondence to the compaction characteristics of the soil, in order to obtain a constant dry density for all the specimens. The mixture was compacted by using a tamper, in a square metal ring of 60 × 60 mm dimensions and 23 mm thickness. Subsequently, the compacted sample was carefully inserted into the modified shear box.

2.3. Direct Shear Test

The conventional DST apparatus was employed to conduct the

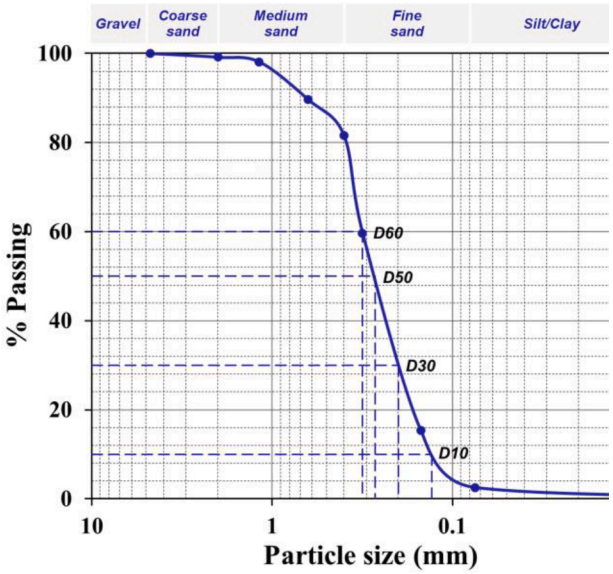

Fig. 1. Particle size distribution of the soil.

Table 1
Soil main properties.

Properties	Symbols	Values
Mean particle diameter	D_{50} (mm)	0.269
Uniformity coefficient	Cu	2.43
Coefficient of curvature	Cc	0.97
Specific gravity	Gs	2.65
Maximum dry density	ρ_d (g/cm^3)	1.6
Optimum moisture content	OMC (%)	10
Cohesion	C (kPa)	4.11
Angle of internal friction	Φ (°)	36.05

experimental investigation, according to ASTM D 3080 [57]. However, one side of the original metal box of 60 × 60 mm dimensions was replaced by a transparent plate; thus, making it possible to visually monitor the soil particles displacement and deformation with a conventional (RGB) camera. In a preliminary approach, a new cost-effective mold was manufactured for experimental purposes by employing a fused deposition modelling (FDM) based 3-D printer, and rigid bioplastic filament. The modified shear box was printed by using solid Polylactic Acid (PLA) with an infill rate of 100% (no voids), whose typical tensile strength varies from 30 to 60 MPa. Although not comparable to steel, the solid PLA material is still rigid enough to efficiently reproduce the considered mold. Additionally, the shape and dimensions of the new box were identical to the original one. Therefore, it is to be expected that the manufactured shear-box will not have any interference with the DST results. The open side of the new box was closed by using two Plexiglass (PMMA; Polymethyl methacrylate) plates of 4 mm thickness screwed to the upper and lower parts of the shear box as illustrated in Fig. 2. Moreover, half of the transparent plexiglass plate was painted with a black/white speckled pattern to acquire a reference area for the intended measurements with DIC. Thus, the in-plane displacements detected by DIC on these reference boards can be directly compared against the shear box displacements registered by the transducers. The adoption of this method was easy, fast, and practical, avoiding the alteration of the soil properties arising from painting the soil grains. Besides, the method could be employed under any moisture condition (dry, wet, or saturated soils), thus increasing the efficiency of the applied speckling technique. Whereas, by speckling the soil particles, only dry conditions could be applied, since the paint on the grain surface will be obviously affected by the humidity, arising more shortcomings.

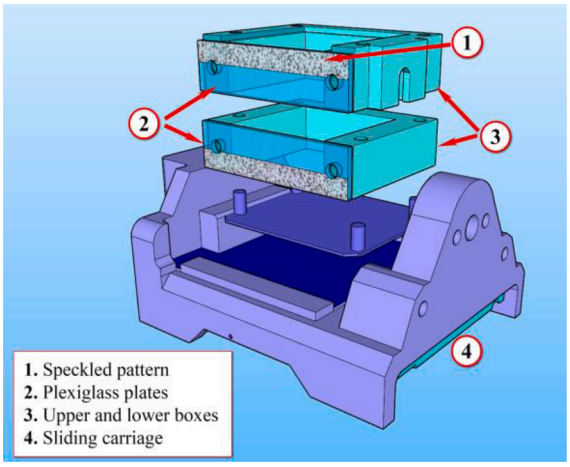

Fig. 2. Model representing the modified shear box and carriage.

The DST was performed under the normal pressures of 100, 200, 300, and 400 kPa and at a shear rate of 0.5 mm/min. The test was ended at 10 mm horizontal displacement, thereby a shear strain greater than 15% had been reached, yet the shear failure took place earlier.

2.4. Digital Image Correlation Set-up

Two-dimensional DIC was applied in this study, given that the examined material has a planar surface and only in-plane measurements are intended to be explored. A single camera was fixed with its optical axis perpendicular to the considered soil surface (Fig. 3). The camera employed is a digital single-lens reflex (DSLR) Canon EOS 1200D, having a resolution of 18.1-megapixel and provided with Canon EF lens (image settings: focal length 21 mm, ISO-100, exposure time 1/25 s, f/6). Cold LED light source was also mounted to illuminate the entire targeted field of view. The lighting intensity and position were adjusted to have sufficient and uniform contrast between the brightest and darkest regions of the pattern. A digital intervalometer was also used to take pictures of the shearing box with a constant frame rate of 0.5 images·s^{-1}.

The series of recorded images were processed by using the software GOM Correlate (GOM GmbH). Non-incremental DIC was chosen as the method of calculation after finding that no correlation issues arose when tracking the sand pattern during shearing. Compared with incremental DIC, direct correlation with the reference image introduces no accumulated error in the measured displacements. The other main parameters of DIC, namely subset size (i.e., window calculation size) and step size (i.e., distance between subsets) were manually adjusted to 40 and

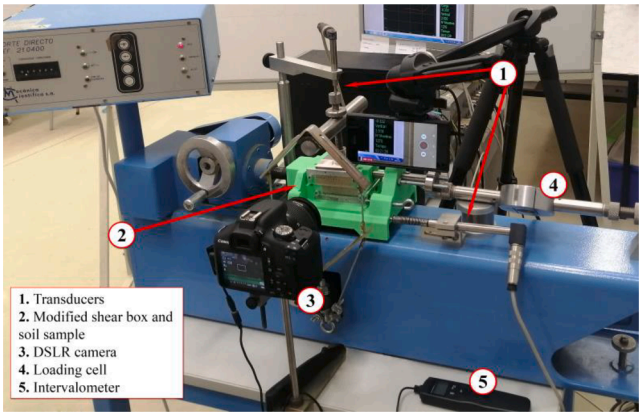

Fig. 3. Experimental set-up of the Direct Shear Test.

18 pixels respectively for all the experiments. These values were chosen in order to obtain an optimized balance between the spatial resolution and the interpolation error. The criterion for setting the subset size value should be to choose a size large enough for a subset to be clearly distinguished from the others, thus minimizing areas with no correlation in the region of interest (ROI). On the other hand, step size influences the spatial resolution of the measurements and is typically two or three times lower than subset size. It should be noted that the smaller the step size is, the longer the calculation time.

3. Results and Discussion

3.1. Analysis of the New Shear Box

In this section, the designed shear box was examined to ensure that the experimental work is run properly without inducing any misrepresentation of the traditional DST. Consequently, the deformation of the plexiglass plate used in the new device, as well as the rotation of the upper shear box and the load cap were analyzed and discussed herein.

3.1.1. Glass Bending Test

The modified shear box should appropriately imitate the mechanical behaviour of the conventional metal box employed in DST. Accordingly, the type and thickness of the Plexiglass plate were assessed, by measuring its lateral deformation when subjected to normal pressure.

The transducer was placed in the middle of the lower plate, which is the critical position, where theoretically the highest lateral deformation could be detected, as illustrated in Fig. 4 (a). The test was performed under static condition (i.e., without shear loading), similar to the consolidation test. The sample was vertically loaded, and the normal stress was gradually increased up to 400 kPa. Another extensometer was positioned at the top of the loading plate to measure the vertical displacement of the soil specimen under the different normal stresses.

It is clear that the vertical displacement of the sample and the lateral deformation of the plate augmented with a further increase in the vertical pressure, as observed in Fig. 4 (b). The maximum lateral bending of the plexiglass attained 0.11 mm at 400 kPa normal stress, which represents 0.183% of the lateral strain in the sample. Accordingly, it could be concluded that the plexiglass plate of 4 mm thickness was suitable for this test showing an insignificant lateral deformation.

3.1.2. Box Rotation Test

The rotation of the shear box and the top-loading plate on the soil sample during DST are some primary reasons for the nonuniformity of stresses. Historically, these criticisms have made geotechnical practitioners skeptical about the reliability of the results of this test [58]. For this reason, it is particularly important to analyze the effect of the modified module on the rotations of the upper box and the loading plate during shearing. Firstly, the inclination of the top part of the box was compared to the one measured in the traditional metal device at a normal pressure of 200 kPa. Secondly, the effect of the applied vertical pressure on the rotation of the new shear box was interpreted. The inclinations were measured with respect to the horizontal axis (X-direction), at a shear strain equal to 15%. Two segments were designated, one on the top edge of the upper shear box, and the other on the top border of the metal loading plate as shown in Fig. 5 (a).

On the one hand, it can be noticed that under the same conditions, the modified shear box rotated more than the original metal device by 10.7% as displayed in Fig. 5 (a) and (b). And the loading head of the newly designed device exhibited a 15.1% increase in inclination when compared to the metal box at 9 mm shear displacement. The cause of this variance is possibly due to the specific gravity of the different materials for each device, given that the metal box has an evidently higher density and stiffness than the plastic one, resulting in less rotation.

On the other hand, the inclination angle increased with increasing the shear displacement as observed in Fig. 6. Moreover, this figure revealed that during shearing, the rotation of the upper part of the specimen augmented with increasing the applied vertical pressure. The lowest inclination of the new box was found at 100 kPa normal stress (1°) and increased by 37.5% at 400 kPa (1.6°). The non-uniform stress

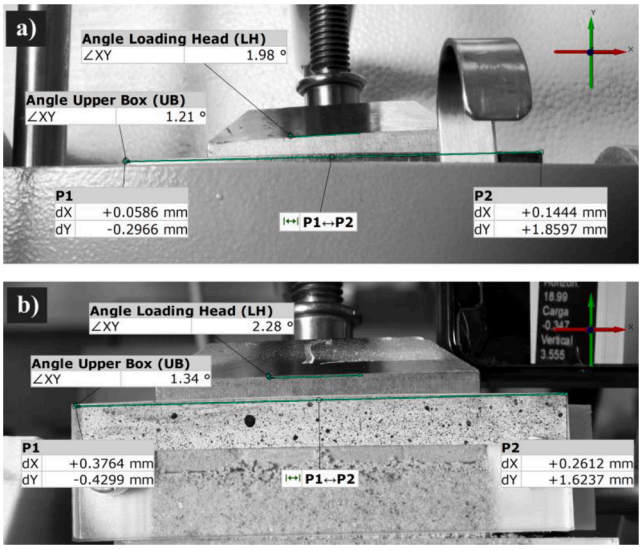

Fig. 5. Rotation of the upper shear box under 200 kPa normal stress and at 15% strain in the DST using: (a) the original metal box, and (b) the modified shear box.

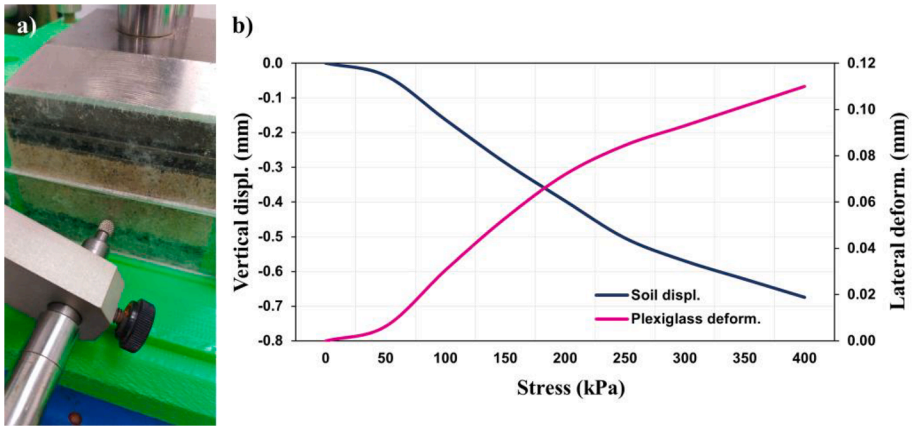

Fig. 4. (a) Transducer position (b) Plexiglass plate deformation and vertical displacement in the sample vs. the applied normal stress.

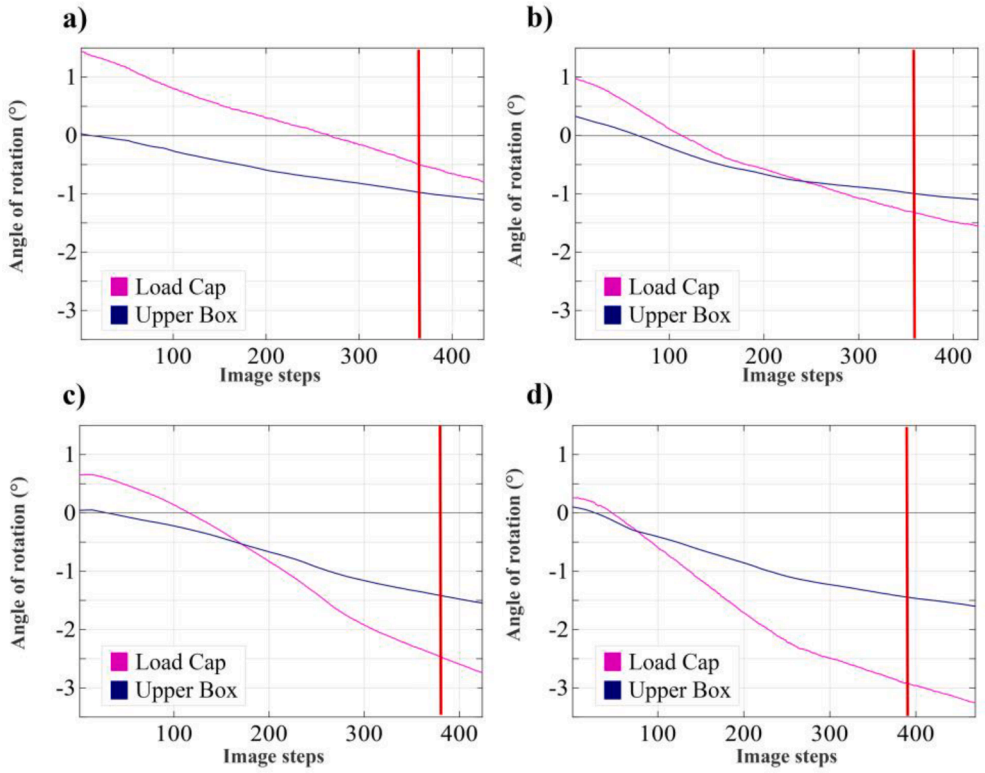

Fig. 6. The inclination angles of the upper modified shear box and loading plate at normal stresses of (a) 100 kPa, (b) 200 kPa, (c) 300 kPa, and (d) 400 kPa. The red vertical lines represent the image step corresponding to 15% shear strain (i.e., 9 mm horizontal displacement).

distribution induced moments and accordingly led to the inclination of the tested specimen. With an ongoing shear displacement, the area of contact in the sample is diminishing, hence, the stresses at the interface increase and the uneven distribution is more pronounced, leading to higher rotation. These findings are in good agreement with other research [59].

It is also worth mentioning that for all the tests, the loading plate rotated more than the upper shear box as illustrated in Fig. 7. Since the load cap is positioned above the soil specimen, its movement is directly influenced by the behaviour of the sand beneath it. The greater rotation could probably be affected by the sample preparation phase, particularly the degree and consistency of compaction of the tested soil. Moreover, this finding could be justified by the initial angles of the load cap which are not set to zero as it is practically difficult, consequently resulting in higher inclination.

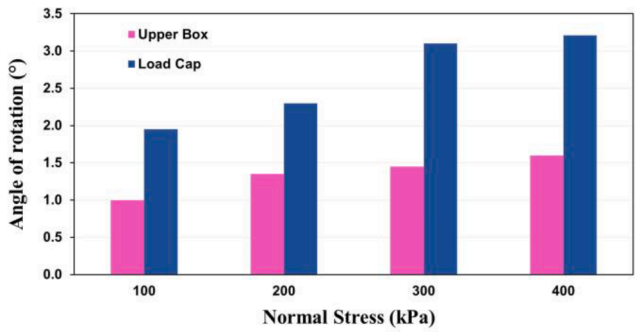

Fig. 7. Variation of rotational angle under different normal pressures at 15% shear strain.

3.2. Analysis of DIC Setup

Quantifying the uncertainty attributed to the image-based method is critical for a rational assessment of the DIC results. The noise floor at the pre-test stage, and the displacement measured by processing the recorded images during the shear stage, were evaluated in this section.

3.2.1. Noise-Floor Analysis

An in-depth revision of the fundamentals, error sources and uncertainty quantification for DIC can be found in previous research [60,61]. Although the error sources in DIC are varied, a common approach for their quantification is the determination of the noise floor. The fundamental concept of the noise-floor analysis, also known as variance error quantification, is to correlate static digital images that were obtained under the same conditions of the conducted test. Therefore, to analyze the noise floor, a series of approximately forty pre-test photos were taken for the static shear box in the unloaded condition. In the image processing, the expectable displacement calculated by DIC technique must be zero, hence any computed displacement is considered noise.

The noise level is normally similar between the horizontal and vertical directions. However, it is advisable to calculate these indicators distinctly for each direction, selecting the maximum or the average between these directions [62]. Therefore, twelve points were designated to perform the noise floor analysis of the planar components in the stationary image series. Three points, on the middle and sides, were chosen on each relevant part (i.e., upper, and lower) of the shear box, in both the speckled and sand ROIs, as observed in Fig. 8. The resulting noise baseline is displayed in Fig. 9 for the selected points in both directions.

The standard deviation (SD) was computed to quantify the variance errors, and it was calculated for the sections of sand and speckled pattern separately. Table 2 summarizes the statistics of the noise analysis for the displacement in the horizontal and vertical directions. It can be noticed that the noise SD for the soil is marginally greater than the painted

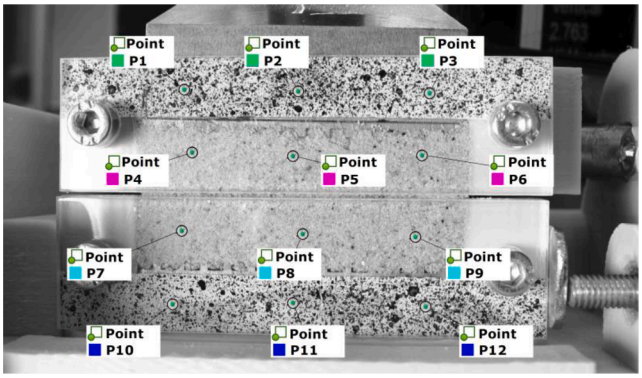

Fig. 8. Selected check points distributed on both sides and at the middle of the upper and lower shear boxes.

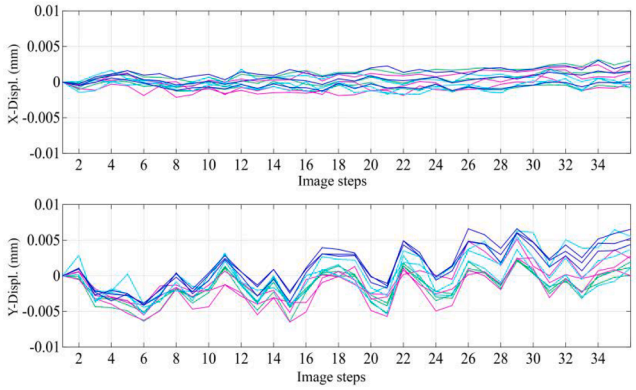

Fig. 9. Variation of baseline noise at 12 checkpoints for (a) horizontal displacement (b) vertical displacement.

Table 2
Overall Statistics for noise floor levels.

Section	Sand section		Speckled section	
Direction	X-displ.	Y-displ.	X-displ.	Y-displ.
Min. (mm)	−0.0054	−0.0131	−0.0027	−0.0064
Max. (mm)	0.006	0.0145	0.0052	0.0084
Mean (mm)	0.00031429	5.7143E-05	0.00032857	0.00027143
SD (mm)	0.00100857	0.00169429	0.00075714	0.00116857

section in both directions. However, the low standard deviation values are indicative of the precision of the applied optical method.

Furthermore, the noise was estimated from a single image step for both horizontal and vertical directions, in order to assess the effect of the considered surface, namely the sand and speckled regions. In this case, two profiles were considered in the lower shear box, highlighted with lines where the corresponding responses are displayed in Fig. 10 (a). It can be perceived that the noise was higher in the soil section than the speckled one for both X and Y directions, as shown in Fig. 10 (b) and (c), respectively. This is reasonable, considering the fact that DIC results are less noisy when using an appropriate stochastic pattern of contrasting features.

3.2.2. Displacement Accuracy Assessment

Although the DIC technique has shown the potential to provide a high accuracy level comparable to contact methods in several previous studies, the precision of DIC using consumer grade equipment (e.g., DSLR cameras) has not been yet fully investigated. In this work, the accuracy is assessed by comparing the horizontal displacements recorded by a conventional contact measurement device (i.e., transducer) to those computed by processing the images with DIC. For the accuracy analysis, two ROIs were selected on the upper and lower shear boxes within the speckled pattern of the plexiglass plate as seen in Fig. 11. The figure exhibited almost a stationary position for the upper box (in blue), however, the lower box displayed an approximately 10 mm horizontal displacement indicating the end of the test.

The relation between the shear displacements obtained by the transducer and the image processing technique exhibited a good fit. And Fig. 12 Percent12presented the percentage of error along with the brief statistics for the difference of horizontal displacements between extensometer and DIC measurements. The graph depicted a low percent error, with an overall [mean (SD)] error of −0.009 (0.026) mm. The fitted results affirmed the accuracy of employing the DIC technique in DST.

3.3. Consolidation Phase

As for the consolidation and shear processes, a new ROI was defined including the whole window of the shearing box corresponding to the sand area. Fig. 13 Particles13represents the consolidation settlement of the soil under an applied normal load of 300 kPa. The grains moved downward rapidly indicating a volumetric compression within the soil. Also, a marginal horizontal displacement of the particles was noticed, it is approximately balanced between the right and left parts of the samples but in opposite directions. However, for granular materials, the squeezing out of water is very quick and the consolidation process takes place in a short time upon load application as seen in Fig. 13 Particles13, 5 s in this case, well known as immediate settlement. Under a specific normal force, the end of the consolidation phase was depicted when the readings of vertical transducer are stabilized. The completion of consolidation was verified by interpreting the plot of the normal displacement versus either log of time or square root of time, as specified in ASTM D 3080 [57], when no additional settlement was noticed.

Fig. 14 The14illustrates the vertical displacement of the particles measured by DIC under two different normal stresses (200 and 400 kPa) at the end of the consolidation phase, or simply when no significant change in the movement was induced by the applied load. The figure also displays the variation in the displacement along five different profiles. It is obvious that the vertical displacement augmented by increasing the normal pressure.

Furthermore, the graphs show that the settlement was more pronounced at the top edge of the box since the downward movement of the lower part was restricted by the motionless base plate. It could be also noticed that the repositioning of the grains was asymmetrical about the vertical center line of all the tested samples. The right sections experienced higher displacement than the left ones. The slight difference could be attributed to the non-homogeneity in soil specimens due to the inability to perfectly ensure an even compacted sample with an exact straight and smooth surface. However, these observations assert the significance of applying DIC to DST, where high precision of vision-based data could be captured.

3.4. Shear Process

Analyzing the DIC planar displacement maps of the soil grains throughout the test generates more profound understanding of the meso-mechanical behaviour of the material. Fig. 15 (a) illustrates the shear stress-horizontal displacement curves of the samples under varying normal pressures of 100, 200, 300, and 400 kPa. Fig. 15 (b) to (f) present the incremental subset displacement diagrams in both X and Y directions at a normal pressure of 300 kPa. In each figure, the upper one indicates the horizontal displacement (dX), while the lower indicates the vertical displacement (dY).

On the one hand, it can be observed that the soil grains in the upper part of the lower shear box experienced less horizontal displacement than those located in the center and bottom parts of it. In fact, the grains in the bottom part moved concurrently with the shear displacement

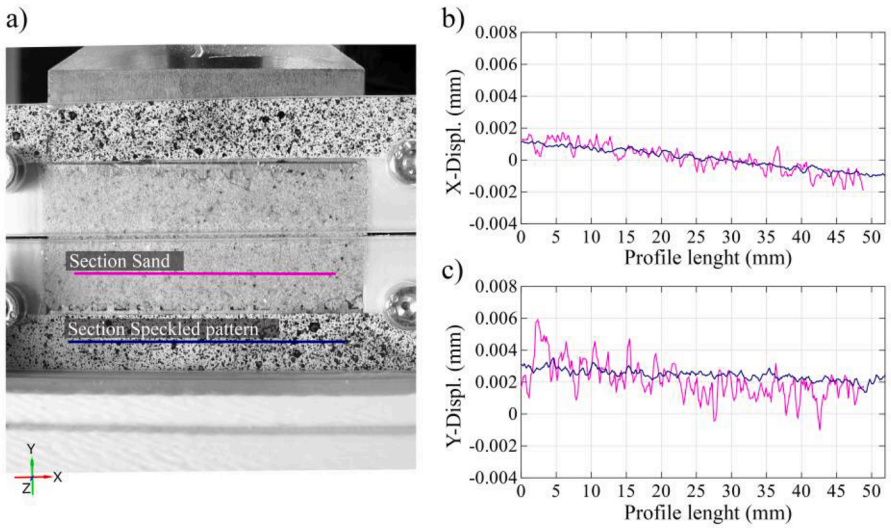

Fig. 10. Noise-floor analysis in one image step (step 18) (a) selected profiles. Baselines noise for (b) horizontal displacement and (c) vertical displacement.

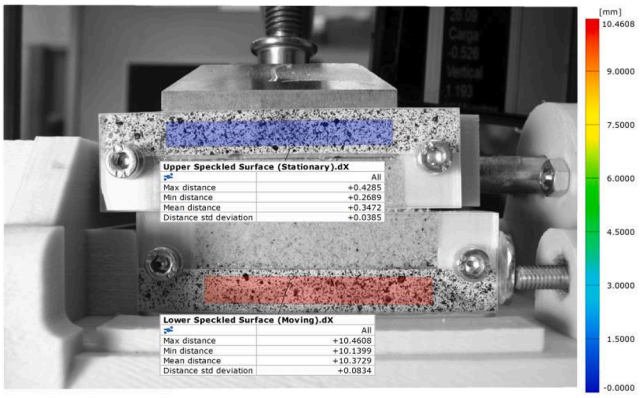

Fig. 11. Shear displacement measured by DIC.

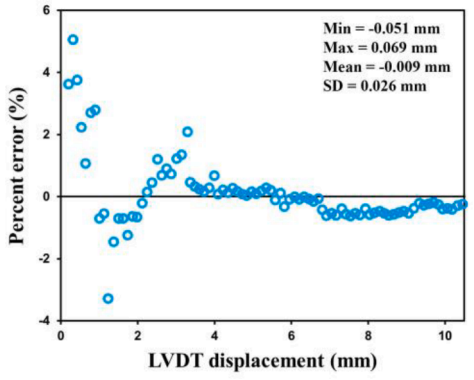

Fig. 12. Percent12 error and brief statistics for the difference of X-displacements computed by extensometer and DIC'.

applied to the lower box, however, the upper portion was affected by the fixed boundary beyond it resulting in less horizontal displacement. Meanwhile, it was also noted that in the middle of the box, a presumptive band was created showing lateral displacement ranging from zero at the upper border of the supposed layer to maximum displacement at its lower border. The development of this layer is called shear band formation and will be discussed later in this research. These observations agree with the findings of other studies [63].

On the other hand, at the start of the shear test, the particles showed non uniform vertical displacement along the X-axis (Points A and B in Fig. 15 (a)). An upward (positive) movement was detected on the right side, while a downward (negative) movement was seen on the left part of the box. As the test continued, the nonuniformity of the normal displacement is rotated counterclockwise to be in some way symmetrical about the diagonal of the box from the upper right to lower left. However, the upward displacement was more perceived, explaining the commonly dilative behaviour of the sandy soil where some particles must slide upon the others during shearing. Moreover, the nonuniformity of the vertical movement is certainly influenced by the rotation of the top cap and the box discussed previously.

Throughout the shear process, the soil particles undergo both translational and rotational movements. The GOM software computes the shear angle from the stretch tensor at several points. Theoretically, at least three points are required (triangle), yet the software uses additional adjacent points to the individual targeted one, for improved verified measurement. Consequently, an equilateral hexagon enclosed by the surface is considered, where the strains must be computed as represented in Fig. 16 (a).

The shear angle maps of the investigated soil are illustrated in Fig. 16 (b) to (f) with a close-up of the shear zone for the same selected points as in Fig. 15 (a). As observed in the next figure, with a further induced horizontal displacement, the shear angle is increased to reach its maximum value at the residual state (Point E). The large shear displacement induced the distortions of the grids at the intersection between the upper and lower boxes. Similar trends were noticed for all the applied normal stresses (100, 200, and 400 kPa).

The analyses of the shear process are based on the observation of in-plane particle behaviour, yet we cannot ignore that out-of-plane interactions also occur during DST. What seems reasonable to state, based on our experiments, is that the out-of-plane displacements were not significant. Otherwise, problems would have been detected in the subset matching process.

3.5. Shear Band Analysis

3.5.1. Strain Localization

Fig. 17 displays the distribution of strain in the samples subjected to 200 and 400 kPa applied normal stresses at three distinct moments, namely, at pre-failure (a and b), at failure where a distinct peak shear stress was exhibited (c and d), and at post-failure (e and f). The DIC software converts the measured surface coordinates into strain values. In this case the major strain was considered, which is the largest possible

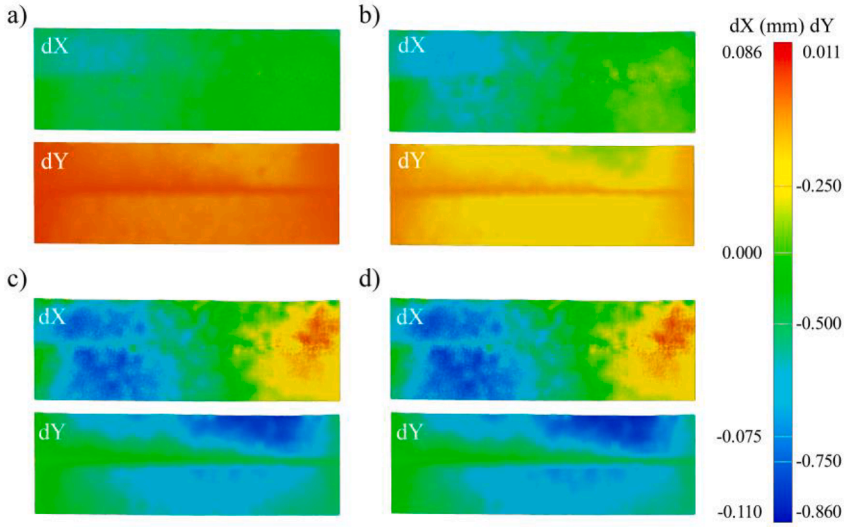

Fig. 13. Particles13 displacement during consolidation phase under 300 kPa normal stress at different time steps: (a) $t = 1$ s, (b) $t = 3$ s, (c) $t = 5$ s, and (d) $t = 9$ s.

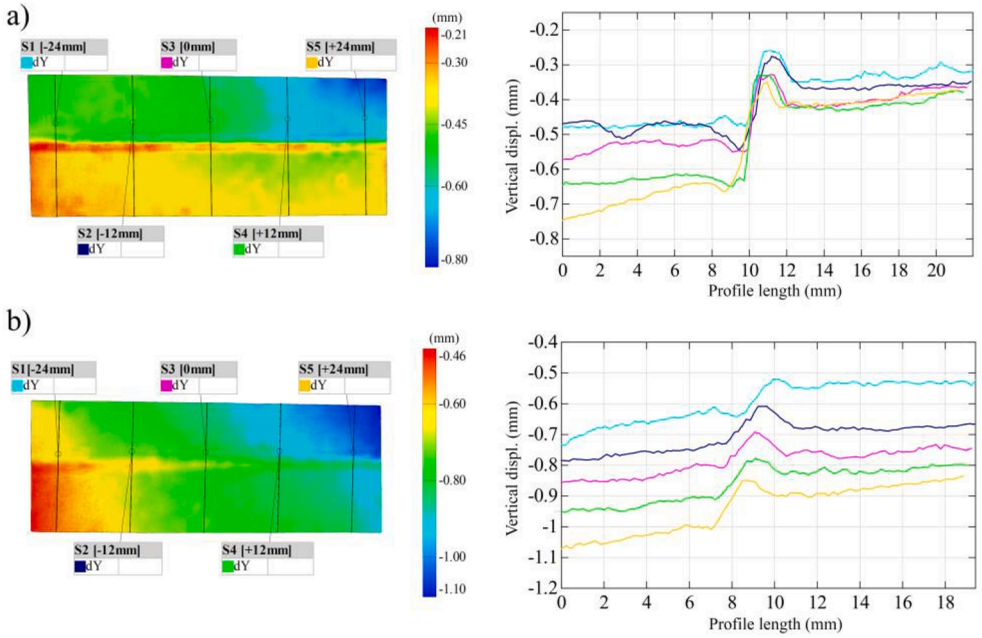

Fig. 14. The14 vertical displacement diagrams of the soil at the end of consolidation stage, and the variation of the displacements along the length of the selected profiles at normal pressures of (a) 200 kPa (b) 400 kPa.

strain of a targeted element. Several points were selected in the upper, middle, and bottom parts of the specimen to quantitatively assess the strain variation. The strains augmented with an increase in the normal stress, particularly in the central zone of the samples for all the phases.

The first studied stage describes the strain localization during the plastic deformation of the sample, this stage follows the elastic phase (linear stress-strain relation) and precedes the failure. It can be noticed that the strain is concentrated within a specified zone around the mid-height of the shear box. This strain localization was developed after the soil particles relocate and rearrange to adapt to the external applied conditions. At this stage, the development of a shear band is well observed at the junction of the upper and lower boxes.

With a further shear displacement, the shear strains within the band increased considerably, and the borders of the shear band became more and more noticeable. These high strain zones propagate in the sample along the horizontal contact area between the boxes. However, as it was observed, the strain changes outside the shear band during the different stages were insignificant. These results are consistent with the findings of other research employing the X-ray-computed tomography (CT) scanner with the DST to investigate the behaviour of sand and tire chips [2]. Similarly to other research [54], during the post-failure phase, the soil experienced a strain-softening behaviour, which is the critical stage where the thickness of the shear band attains almost a constant value.

3.5.2. *Shear Band Thickness*

The shear band behaviour has long been an essential concern to properly interpret the response of soil and to quantify the local strain development. One important physical characteristic of the shear band is the thickness that could be successfully estimated with the DIC approach. It is generally calculated with respect to the mean grain diameter (D_{50}).

Eleven profiles were taken along the sample height as it is shown in

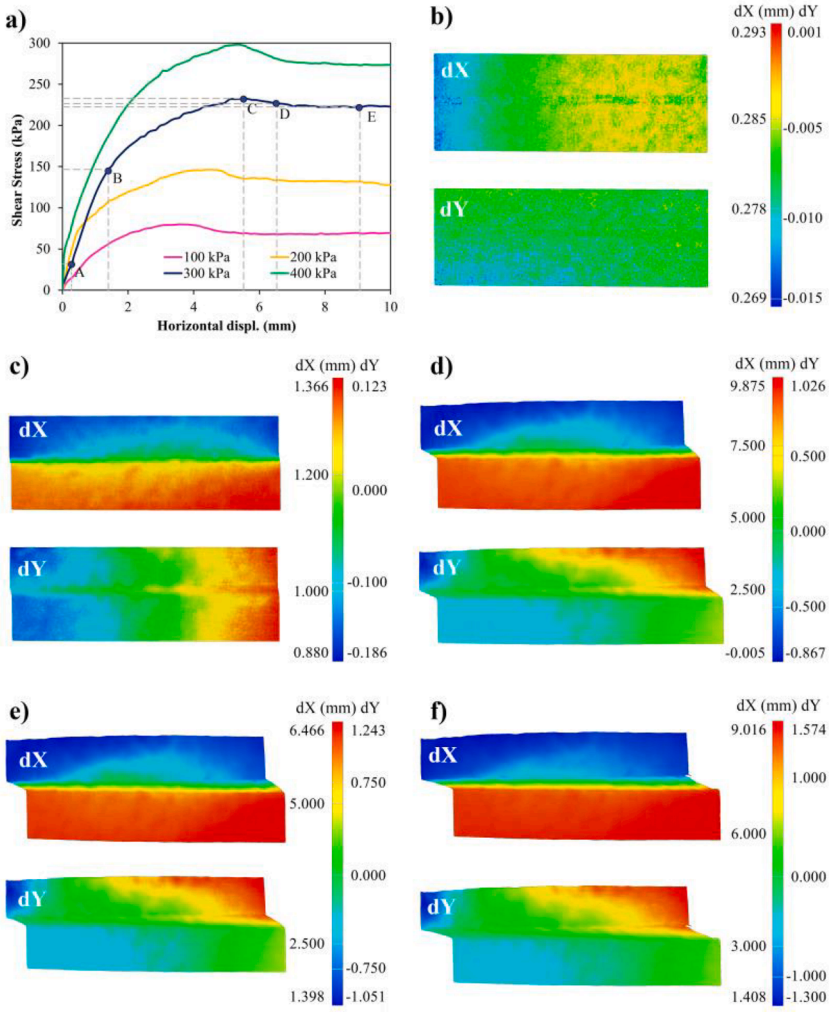

Fig. 15. (a) Shear stress-displacement curves at different vertical pressures (b)-(f) Horizontal and vertical displacement maps at 300 kPa normal stress for (b) Point A, (c) Point B, (d) Point C, (e) Point D, and (f) Point E.

Fig. 18 (a) and perpendicular to the shear band to precisely estimate its thickness. The strain values are obtained along these sections as displayed in Fig. 18 (a). Subsequently, the mean curve of the strains was also estimated and presented in Fig. 18 (b). The thickness of the shear band is considered as the distance between the points having the maximum gradient in the average curve. Moreover, Fig. 18 (c) summarized the calculated shear band thickness under varying vertical loads, along with the normalized shear band thickness (t/D_{50}).

The results showed that the shear band thickness ranged between 11.5 and 11.9D_{50}. Previous experimental study of ring shear test performed on three types of sand has shown that the ratio of the shear band thickness to D_{50} is equal to 10 for poorly graded sands and 14 for silty sand [64]. Furthermore, previous research [65] investigated the shear band thickness under plane strain loading conditions for different types of sandy soil. They stated that the range of the ratio between the thickness and D_{50} is 10 to 11 for coarse sand, 11 to 12 for medium grained sand, and 13 to 14 for fine sand.

It is also noteworthy that the thickness slightly rose with an increase of the normal stress. The increase in the confining or vertical pressure caused higher strain values in the middle of the specimens, as it was demonstrated previously. These greater strains propagate and localize over a relatively larger zone in the granular material. Consequently, this explains the marginal increase of the shear band thickness.

4. Conclusions

The shear behaviour of poorly graded sand in DST was investigated by employing 2D-DIC processing under different vertical stresses of 100, 200, 300, and 400 kPa. A new cost-effective 3D printed shear box was created to visually monitor the meso-mechanical behaviour of the soil. The optical approach was demonstrated to be an effective tool not only to visualize the results but particularly to quantify the measurements such as strains and displacements during DST.

The potential application of DIC to DST was successfully validated by assessing the noise-floor of the pre-test stationary images, and by comparing the shear displacement to the one measured by a transducer. Additionally, the use of the newly designed shear box was demonstrated to be suitable for performing the DST test, by measuring the deformation of the plexiglass plates of the new device and by evaluating the rotation of the upper box and the load cap.

In the consolidation stage, the immediate settlement of the granular material was observed. During shearing, the vertical movement inside the sample explained the dilation behaviour of the compacted siliceous sand. Moreover, we used partially saturated samples, and under these conditions no imaging artifacts were detected. However, it would be interesting to investigate the possible application of the method using samples with a high degree of saturation or even submerged samples. DIC application on DST also opens up new possibilities for quantifying shear expansion at different test phases and monitoring how this

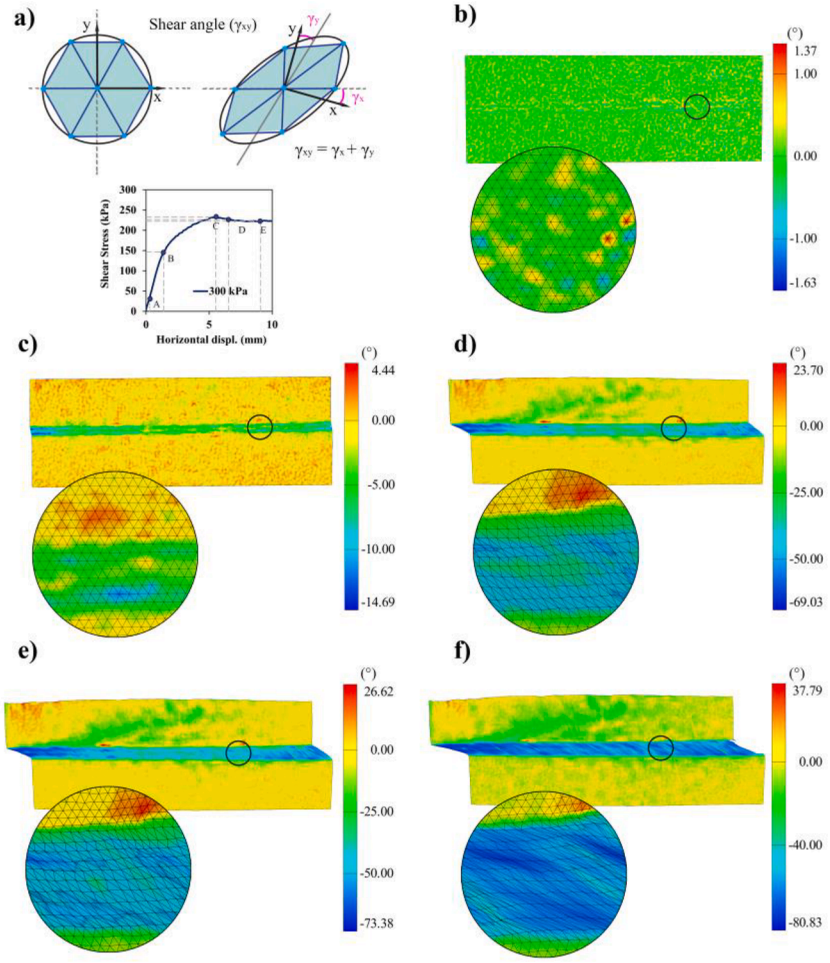

Fig. 16. (a) Schematic representation of the shear angle (b)-(f) Shear angle maps at 300 kPa vertical pressure with a detailed view of the shearing zone for (b) Point A, (c) Point B, (d) Point C, (e) Point D, and (f) Point E.

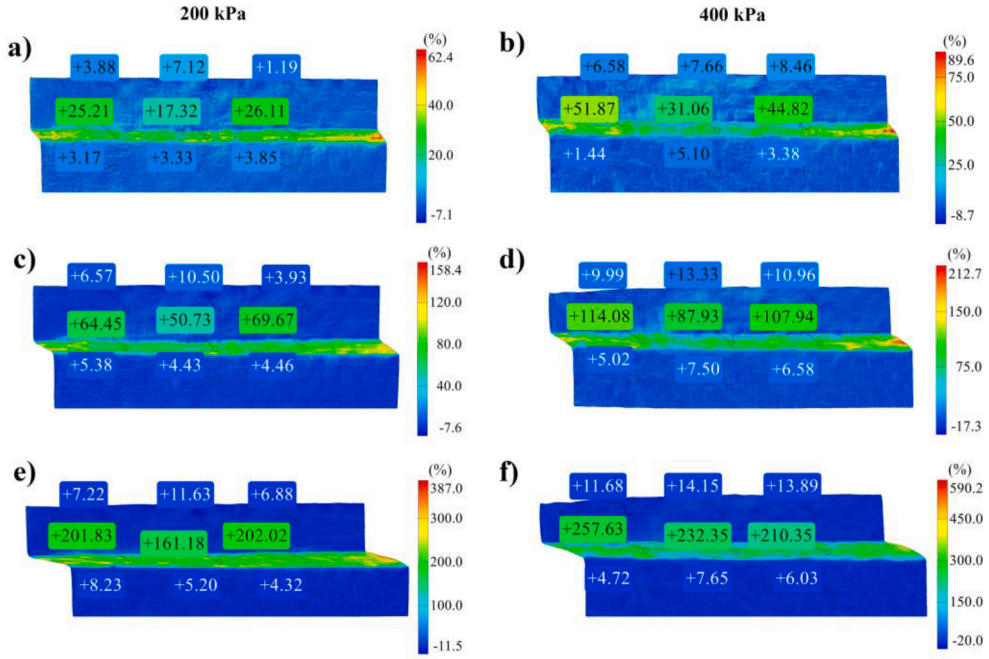

Fig. 17. Shear strain distribution under 200 and 400 kPa vertical pressures at different stages: (a)-(b) pre-failure, (c)-(d) failure, and (e)-(f) post-failure.

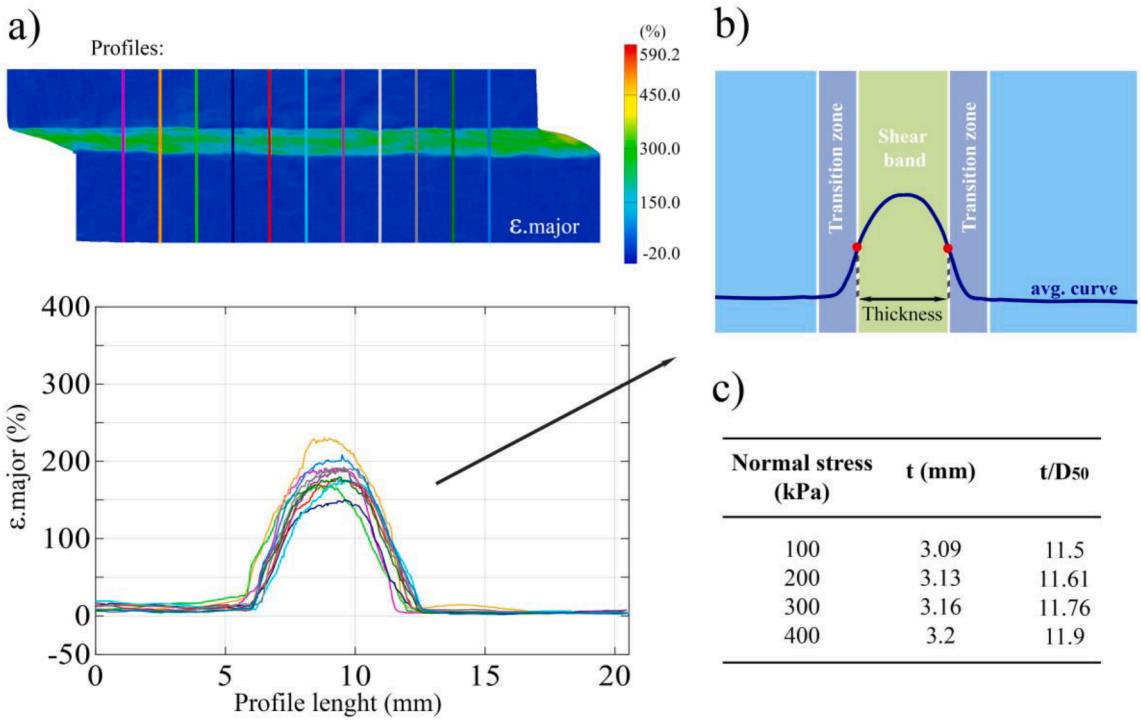

c)

Normal stress (kPa)	t (mm)	t/D50
100	3.09	11.5
200	3.13	11.61
300	3.16	11.76
400	3.2	11.9

Fig. 18. Shear band thickness estimation (a) Vertical strain distribution along the selected sections, (b) Mean strain curve, (c) Shear band thickness values for different normal pressures.

phenomenon varies under different normal stresses, yet further research is still needed on this point.

Furthermore, the localization of strain was propagated at the junction of the upper and lower shear boxes. A clear shear band was formed at this interface, and the ratio between the band thickness to the mean grain diameter reached a value of 11.5 and slightly increased to 11.9 under normal stresses of 100 and 400 kPa, respectively. In the tests performed, the thickness of the shear band increases with shear displacement. While the justification for the occurrence of this phenomenon exceeds the scope of this paper, which could be investigated by means of DIC in future works. The results of this study demonstrated that the employment of DIC was highly effective and suitable and could overcome the main limitations of the conventional DST where the non-uniformity and the localization of the strains could not be examined.

CRediT authorship contribution statement

G. Alhakim: Investigation, Visualization, Writing – original draft. **C. Núñez-Temes:** Resources, Conceptualization, Validation. **J. Ortiz-Sanz:** Methodology, Supervision. **M. Arza-García:** Methodology, Software, Writing – review & editing. **Lina Jaber:** Writing – review & editing. **M.L. Gil-Docampo:** Conceptualization, Project administration.

Declaration of Competing Interest

The authors declare that they have no known competing financial interests or personal relationships that could have appeared to influence the work reported in this paper.

Data availability

Data will be made available on request.

Acknowledgments

This work was supported by the regional government of Galicia (Xunta de Galicia, Spain) under the grant “Financial aid for the consolidation and structure of competitive units of investigation in the universities of the University Galician System (2020-22)” Ref. ED341B 2020/25. The work was also supported by the individual grants of the EU Commission under the program Erasmus+ KA107 with a mobility grant awarded to Ghida Alhakim and by the Xunta de Galicia with the postdoctoral grant awarded to Marcos Arza-García (ED481B 2022/075).

References

[1] A. Eslami, S. Moshfeghi, H. MolaAbasi, M.M. Eslami, Background to foundation engineering, in: Piezocone Cone Penetration Test (CPTu CPT) Appl. Found. Eng, 2020, pp. 25–53, https://doi.org/10.1016/b978-0-08-102766-0.00002-x.
[2] B. Chevalier, Y. Tsutsumi, J. Otani, Direct shear behavior of a mixture of sand and tire chips using X-ray computed tomography and discrete element method, Int. J. Geosynth. Gr. Eng. 5 (2019) 1–12, https://doi.org/10.1007/s40891-019-0160-3.
[3] J. Kozicki, M. Niedostatkiewicz, J. Tejchman, H.B. Muhlhaus, Discrete modelling results of a direct shear test for granular materials versus FE results, Granul. Matter 15 (2013) 607–627, https://doi.org/10.1007/s10035-013-0423-y.
[4] A. Simoni, G.T. Houlsby, The direct shear strength and dilatancy of sand-gravel mixtures, Geotech. Geol. Eng. 24 (2006) 523–549, https://doi.org/10.1007/s10706-004-5832-6.
[5] P.K. Wu, K. Matsushima, F. Tatsuoka, Effects of specimen size and some other factors on the strength and deformation of granular soil in direct shear tests, Geotech. Test. J. 31 (2008) 45–64, https://doi.org/10.1520/gtj100773.
[6] M. Nitka, A. Grabowski, Shear band evolution phenomena in direct shear test modelled with DEM, Powder Technol. 391 (2021) 369–384, https://doi.org/10.1016/j.powtec.2021.06.025.
[7] W.J. Xu, G.Y. Liu, H. Yang, Study on the mechanical behavior of sands using 3D discrete element method with realistic particle models, Acta Geotech. 15 (2020) 2813–2828, https://doi.org/10.1007/s11440-020-00982-0.
[8] M. Jiang, J. Liu, Z. Shen, B. Xi, Exploring the critical state properties and major principal stress rotation of sand in direct shear test using the distinct element method, Granul. Matter 20 (2018) 1–18, https://doi.org/10.1007/s10035-018-0796-z.
[9] C. Wang, A. Deng, A. Taheri, Three-dimensional discrete element modeling of direct shear test for granular rubber–sand, Comput. Geotech. 97 (2018) 204–216, https://doi.org/10.1016/j.compgeo.2018.01.014.
[10] S. Zhao, X. Zhou, W. Liu, Discrete element simulations of direct shear tests with particle angularity effect, Granul. Matter 17 (2015) 793–806, https://doi.org/10.1007/s10035-015-0593-x.
[11] W.M. Yan, Fabric evolution in a numerical direct shear test, Comput. Geotech. 36 (2009) 597–603, https://doi.org/10.1016/j.compgeo.2008.09.007.

[12] S. Lobo-Guerrero, L.E. Vallejo, Discrete element method evaluation of granular crushing under direct shear test conditions, J. Geotech. Geoenviron. Eng. 131 (2005) 1295–1300, https://doi.org/10.1061/(asce)1090-0241(2005)131:10(1295).
[13] C. Thornton, L. Zhang, Numerical simulations of the direct shear test, Chem. Eng. Technol. 26 (2003) 153–156.
[14] M. Wiebicke, E. Andò, G. Viggiani, I. Herle, Measuring the evolution of contact fabric in shear bands with X-ray tomography, Acta Geotech. 15 (2020) 79–93, https://doi.org/10.1007/s11440-019-00869-9.
[15] L. Babout, K. Grudzień, J. Wiącek, M. Niedostatkiewicz, B. Karpiński, M. Szkodo, Selection of material for X-ray tomography analysis and DEM simulations: comparison between granular materials of biological and non-biological origins, Granul. Matter 20 (2018), https://doi.org/10.1007/s10035-018-0809-y.
[16] D. Takano, N. Lenoir, J. Otani, S.A. Hall, Localised deformation in a wide-grained sand under triaxial compression revealed by X-ray tomography and digital image correlation, Soils Found. 55 (2015) 906–915, https://doi.org/10.1016/j.sandf.2015.06.020.
[17] I. Vlahinić, E. Andò, G. Viggiani, J.E. Andrade, Towards a more accurate characterization of granular media: extracting quantitative descriptors from tomographic images, Granul. Matter 16 (2014) 9–21, https://doi.org/10.1007/s10035-013-0460-6.
[18] E. Andò, G. Viggiani, S.A. Hall, J. Desrues, Experimental micro-mechanics of granular media studied by x-ray tomography: recent results and challenges, Geotech. Lett. 3 (2013) 142–146, https://doi.org/10.1680/geolett.13.00036.
[19] S.A. Hall, J. Desrues, G. Viggiani, P. Bésuelle, E. Andò, Experimental characterisation of (localised) deformation phenomena in granular geomaterials from sample down to inter-and intra-grain scales, Procedia IUTAM 4 (2012) 54–65, https://doi.org/10.1016/j.piutam.2012.05.007.
[20] B.S.A. Tatone, G. Grasselli, Characterization of the effect of normal load on the discontinuity morphology in direct shear specimens using X-ray micro-CT, Acta Geotech. 10 (2015) 31–54, https://doi.org/10.1007/s11440-014-0320-5.
[21] M. Jastrzębska, Modern displacement measuring systems used in geotechnical laboratories: advantages and disadvantages, Sensors. 21 (2021), https://doi.org/10.3390/s21124139.
[22] N. Vanderesse, A. Richter, N. Nuño, P. Bocher, Measurement of deformation heterogeneities in additive manufactured lattice materials by digital image correlation: strain maps analysis and reliability assessment, J. Mech. Behav. Biomed. Mater. 86 (2018) 397–408, https://doi.org/10.1016/j.jmbbm.2018.07.010.
[23] T.C. Chu, W.F. Ranson, M.A. Sutton, Applications of digital-image-correlation techniques to experimental mechanics, Exp. Mech. 25 (1985) 232–244, https://doi.org/10.1007/BF02325092.
[24] W.H. Peters, W.F. Ranson, Digital imaging techniques in experimental stress analysis, Opt. Eng. 21 (1982) 427–431.
[25] F. Abbassi, F. Ahmad, Behavior analysis of concrete with recycled tire rubber as aggregate using 3D-digital image correlation, J. Clean. Prod. 274 (2020), 123074, https://doi.org/10.1016/j.jclepro.2020.123074.
[26] J. Mata-Falcón, S. Haefliger, M. Lee, T. Galkovski, N. Gehri, Combined application of distributed fibre optical and digital image correlation measurements to structural concrete experiments, Eng. Struct. 225 (2020), https://doi.org/10.1016/j.engstruct.2020.111309.
[27] N. Gehri, J. Mata-Falcón, W. Kaufmann, Refined extraction of crack characteristics in large-scale concrete experiments based on digital image correlation, Eng. Struct. 251 (2022), https://doi.org/10.1016/j.engstruct.2021.113486.
[28] S. Meng, C. Jiao, X. Ouyang, Y. Niu, J. Fu, Effect of steel fiber-volume fraction and distribution on flexural behavior of ultra-high performance fiber reinforced concrete by digital image correlation technique, Constr. Build. Mater. 320 (2022), 126281, https://doi.org/10.1016/j.conbuildmat.2021.126281.
[29] C. Lakavath, S.S. Joshi, S.S. Prakash, Investigation of the effect of steel fibers on the shear crack-opening and crack-slip behavior of prestressed concrete beams using digital image correlation, Eng. Struct. 193 (2019) 28–42, https://doi.org/10.1016/j.engstruct.2019.05.030.
[30] J.F. Destrebecq, E. Toussaint, E. Ferrier, Analysis of cracks and deformations in a full scale reinforced concrete beam using a digital image correlation technique, Exp. Mech. 51 (2011) 879–890, https://doi.org/10.1007/s11340-010-9384-9.
[31] T.M. Fayyad, J.M. Lees, Application of digital image correlation to reinforced concrete fracture, Procedia Mater. Sci. 3 (2014) 1585–1590, https://doi.org/10.1016/j.mspro.2014.06.256.
[32] G.L. Golewski, Measurement of fracture mechanics parameters of concrete containing fly ash thanks to use of digital image correlation (DIC) method, Meas. J. Int. Meas. Confed. 135 (2019) 96–105, https://doi.org/10.1016/j.measurement.2018.11.032.
[33] Z. Tang, W. Li, Q. Peng, V.W.Y. Tam, K. Wang, Study on the failure mechanism of geopolymeric recycled concrete using digital image correlation method, J. Sustain. Cem. Mater. 11 (2022) 161–180, https://doi.org/10.1080/21650373.2021.1897706.
[34] L. Cheng, L. Zhang, X. Liu, F. Yuan, Y. Ma, Y. Sun, Evaluation of the fatigue properties for the long-term service asphalt pavement using the semi-circular bending tests and stereo digital image correlation technique, Constr. Build. Mater. 317 (2022), 126119, https://doi.org/10.1016/j.conbuildmat.2021.126119.
[35] N. Sudarsanan, A. Arulrajah, R. Karpurapu, V. Amrithalingam, Digital image correlation technique for measurement of surface strains in reinforced asphalt concrete beams under fatigue loading, J. Mater. Civ. Eng. 31 (2019) 1–10, https://doi.org/10.1061/(asce)mt.1943-5533.0002743.
[36] C. Núñez-Temes, G. Bastos, M. Arza-García, A. Castro, J.A. Lorenzana Fernández, J. Ortiz-Sanz, M. Portela, M. Gil-Docampo, F.J. Prego, Assessment of pavement deflection under vehicle loads using a 3D-DIC system in the field, Sci. Rep. 12 (2022) 1–15, https://doi.org/10.1038/s41598-022-13176-3.
[37] G.N. Eichhorn, A. Bowman, S.K. Haigh, S. Stanier, Low-cost digital image correlation and strain measurement for geotechnical applications, Strain. 56 (2020) 1–15, https://doi.org/10.1111/str.12348.
[38] M. Arza-García, C. Núñez-Temes, J.A. Lorenzana, J. Ortiz-Sanz, A. Castro, M. Portela-Barral, M. Gil-Docampo, G. Bastos, Evaluation of a low-cost approach to 2-D digital image correlation vs. a commercial stereo-DIC system in Brazilian testing of soil specimens, Arch. Civ. Mech. Eng. 22 (2022), https://doi.org/10.1007/s43452-021-00325-0.
[39] O. Plé, A. Tourabi, M.S. Abuaisha, 3-dimensional digital image correlation for strains determination in clayey soil, Appl. Mech. Mater. 353–354 (2013) 463–466, https://doi.org/10.4028/www.scientific.net/AMM.353-356.463.
[40] W. Wang, Y. Ye, Q. Wang, N. Hu, Experimental study on anisotropy of strength, deformation and damage evolution of contact zone composite rock with DIC and AE techniques, Rock Mech. Rock. Eng. 55 (2022) 837–853, https://doi.org/10.1007/s00603-021-02682-x.
[41] Y. Cheng, Z. Song, T. Yang, J. Han, B. Wang, Z. Zhang, Investigation on aging deformation and damage mechanics characteristics of layered hard sandstone based on digital image correlation (Dic) technology, SSRN Electron. J. (2022) 8–9, https://doi.org/10.2139/ssrn.4088104.
[42] S. Miao, P.Z. Pan, S. Li, J. Chen, P. Konicek, Quantitative fracture analysis of hard rock containing double infilling flaws with a novel DIC-based method, Eng. Fract. Mech. 252 (2021), 107846, https://doi.org/10.1016/j.engfracmech.2021.107846.
[43] J. Xu, X.Z. Song, S.J. Peng, C.C. Chen, X.M. Ran, F.Z. Yan, Experimental study of generalized stress relaxation of rock based on 3D-DIC technology, Yantu Lixue/Rock Soil Mech. 42 (2021) 27–38, https://doi.org/10.16285/j.rsm.2020.0816.
[44] K. Zhang, F.F. Qi, Y.L. Chen, Deformation and fracturing characteristics of fracture network model and influence of filling based on 3D printing and DIC technologies, Yantu Lixue/Rock Soil Mech. 41 (2020) 2555–2563, https://doi.org/10.16285/j.rsm.2019.1625.
[45] H. Da Li, C.S. Tang, Q. Cheng, S.J. Li, X.P. Gong, B. Shi, Tensile strength of clayey soil and the strain analysis based on image processing techniques, Eng. Geol. 253 (2019) 137–148, https://doi.org/10.1016/j.enggeo.2019.03.017.
[46] P. Wang, Y. Sang, L. Shao, X. Guo, Measurement of the deformation of sand in a plane strain compression experiment using incremental digital image correlation, Acta Geotech. 14 (2019) 547–557, https://doi.org/10.1007/s11440-018-0676-z.
[47] Y. Chen, J. Xu, S. Peng, Q. Zhang, C. Chen, Strain localisation and seepage characteristics of rock under triaxial compression by 3D digital image correlation, Int. J. Rock Mech. Min. Sci. 152 (2022), 105064, https://doi.org/10.1016/j.ijrmms.2022.105064.
[48] Y. Zhu, Z. Medina-Cetina, A.R. Pineda-Contreras, Spatio-temporal statistical characterization of boundary kinematic phenomena of triaxial sand specimens, Materials (Basel) 15 (2022), https://doi.org/10.3390/ma15062189.
[49] L. Li, P. Li, Y. Cai, Y. Lu, Visualization of non-uniform soil deformation during triaxial testing, Acta Geotech. 16 (2021) 3439–3454, https://doi.org/10.1007/s11440-021-01310-w.
[50] S. Fayek, X. Xia, L. Li, X. Zhang, Photogrammetry-based method to determine the absolute volume of soil specimen during triaxial testing, Transp. Res. Rec. 2674 (2020) 206–218, https://doi.org/10.1177/0361198120928339.
[51] P. Wang, X. Guo, Y. Sang, L. Shao, Z. Yin, Y. Wang, Measurement of local and volumetric deformation in geotechnical triaxial testing using 3D-digital image correlation and a subpixel edge detection algorithm, Acta Geotech. 15 (2020) 2891–2904, https://doi.org/10.1007/s11440-020-00975-z.
[52] X. Ji, X. Kong, D. Zou, Y. Sang, C. Zhou, J. Liu, J. Zhao, Measurement of membrane penetration in triaxial specimen through digital image correlation, Acta Geotech. 16 (2021) 1–19, https://doi.org/10.1007/s11440-020-00998-6.
[53] X. Zhang, L. Li, X. Xia, Recent advances in volume measurements of soil specimen during triaxial testing, in: 7th Asia-Pacific Conf. Unsaturated Soils, AP-UNSAT 2019. M, 2019, pp. 31–37, https://doi.org/10.3208/jgssp.v07.004.
[54] J. Shen, X. Wang, W. Liu, P. Zhang, C. Zhu, X. Wang, Experimental study on mesoscopic shear behavior of calcareous sand material with digital imaging approach, Adv. Civ. Eng. 2020 (2020), https://doi.org/10.1155/2020/8881264.
[55] L. Kong, F. Chen, L. Hua, Meso-Direct-Shear Test of Sands Based on the Digital Image Method, 2014, pp. 265–274, https://doi.org/10.1061/9780784413388.027.
[56] B. Pan, K. Qian, H. Xie, A. Asundi, Two-dimensional digital image correlation for in-plane displacement and strain measurement: a review, Meas. Sci. Technol. 20 (2009), https://doi.org/10.1088/0957-0233/20/6/062001.
[57] ASTM, Standard Test Method for Direct Shear Test of Soils under Consolidated Drained Conditions, D3080/D3080M, 2011.
[58] P. Vangla, M.L. Gali, Image-segmentation technique to analyze deformation profiles in different direct shear tests, Geotech. Test. J. 37 (2014), https://doi.org/10.1520/GTJ20130138.
[59] W. Dang, H. Konietzky, T. Frühwirt, Rotation and stress changes on a plane joint during direct shear tests, Int. J. Rock Mech. Min. Sci. 89 (2016) 129–135, https://doi.org/10.1016/j.ijrmms.2016.09.004.
[60] M.G.R. Sause, M.G.R. Sause, Digital image correlation, in: Situ Monit. Fiber-Reinforced Compos. Theory, Basic Concepts, Methods, Appl, 2016, pp. 57–129.
[61] T. Siebert, E. Hack, G. Lampeas, E.A. Patterson, K. Splitthof, Uncertainty quantification for DIC displacement measurements in industrial environments, Exp. Tech. 45 (2021) 685–694, https://doi.org/10.1007/s40799-021-00447-3.
[62] IDICS, A Good Practices Guide for Digital Image Correlation, Int. Digit. Image Correl. Soc, 2018, p. 94, https://doi.org/10.32720/idics/gpg.ed1.%0Ahttp://idics.org/guide/.
[63] S.M. Seyyedan, A.A. Mirghasemi, S. Mohammadi, Numerical simulation of direct shear test on granular materials composed of breakable angular particles: a DEM-

XFEM approach, Powder Technol. 391 (2021) 450–466, https://doi.org/10.1016/j.powtec.2021.06.038.
[64] A. Sadrekamiri, S. Olson, Shear band formation observed in ring shear tests on sandy soils, J. Geotech. Geoenviron. Eng. (2010) 366–375.
[65] K.A. Alshibli, S. Sture, Sand shear band thickness measurements by digital imaging techniques, J. Comput. Civ. Eng. 13 (1999) 103–109, https://doi.org/10.1061/(asce)0887-3801(1999)13:2(103).